# Low-Cost Method for Internal Surface Roughness Reduction of Additively Manufactured All-Metal Waveguide Components

Jakub Sorocki, *Senior Member, IEEE*, Ilona Piekarz, *Senior Member, IEEE*, Michal Baranowski, *Graduate Student Member, IEEE*, Adam Lamecki, *Senior Member, IEEE*, Alberto Cattenone, Stefania Marconi, Gianluca Alaimo, Nicolo Delmonte, *Member, IEEE*, Lorenzo Silvestri, *Member, IEEE*, and Maurizio Bozzi, *Fellow, IEEE*

***Abstract*— In this study, a novel low-cost polishing method for internal surface roughness reduction of additively manufactured components, developed for waveguide (WG) circuits operating in the millimeter frequency range is proposed. WG components fabricated using powder bed fusion (PBF) generally feature roughness of ten to fifty microns, which influences the increase of roughness-related conductor power losses having a major effect on the electrical performance of additively manufactured all-metal WGs. To improve and decrease the surface roughness of circuits fabricated using PBF, glass microbeads as an abrasive medium are proposed to be used in combination with a rotary tumbler. This technique allows the abrasive medium to efficiently penetrate internal long channels and cavities, having cross section dimensions in the range of sub- to a few millimeters. An experimental study was carried out on an example of WG sections and bandpass filters fabricated using PBF through selective laser melting (SLM), operating within the 8.2 to 40 GHz range. Polishing impact on both mechanical and electrical properties was studied showing surface roughness reduction by 18% and sixth order filter's insertion loss reduction at 23 GHz by 40% after 24 h of tumbling with 300–400 $\mu$m large glass microbeads.**

***Index Terms*— Additive manufacturing (AM), all-metal waveguide (WG), glass microbeads, mm-wave electronics, power losses, surface polishing, surface roughness, tumbling, WG.**

Manuscript received 15 October 2023; revised 25 December 2023 and 29 January 2024; accepted 30 January 2024. Date of publication 12 February 2024; date of current version 7 August 2024. The work of Jakub Sorocki and Ilona Piekarz was supported by the National Science Centre, Poland, under Grant 2019/34/E/ST7/00342. The work of Michal Baranowski and Adam Lamecki was supported by the National Science Centre, Poland, under Grant 2020/39/O/ST7/02897. *(Corresponding author: Jakub Sorocki.)*

Jakub Sorocki and Ilona Piekarz are with the Institute of Electronics, AGH University of Krakow, 30-059 Krakow, Poland (e-mail: jakub.sorocki@agh.edu.pl).

Michal Baranowski and Adam Lamecki are with the Department of Microwave and Antenna Engineering, Gdansk University of Technology, 80-233 Gdansk, Poland.

Alberto Cattenone, Stefania Marconi, and Gianluca Alaimo are with the Department of Civil Engineering and Architecture, University of Pavia, 27100 Pavia, Italy.

Nicolo Delmonte, Lorenzo Silvestri, and Maurizio Bozzi are with the Department of Electrical, Computer and Biomedical Engineering, University of Pavia, 27100 Pavia, Italy.

Color versions of one or more figures in this article are available at https://doi.org/10.1109/TMTT.2024.3361976.

Digital Object Identifier 10.1109/TMTT.2024.3361976

## I. Introduction

INCREASING demand for wireless communication systems throughput has been observed in recent years, which requires more efficient use of available resources [1], [2]. Extensive research efforts are directed toward the development of novel solutions and technologies allowing highly integrated and energy-efficient front-end production. A wide range of basic microwave building blocks such as: 1) filters [3], [4]; 2) power dividing/combining networks [5], [6]; 3) frequency multiplexers [7], [8]; and 4) antennas and antenna arrays' feeding networks [6], [9], and so on, are realized in strip transmission line and/or substrate integrated waveguide (SIW) techniques, all made with subtractive techniques. Despite many advantages, such circuits suffer from relatively high power loss being a combination of dielectric, conductor, and radiated losses. Low-loss passive devices are commonly produced with the all-metal waveguide (WG) technique [10], [11], where the wave propagates in lossless air, while attenuation is only due to the finite effective conductivity (combination of bulk conductivity, surface roughness, and frequency of operation) of the metallic walls. However, the main drawback of WG techniques relates to the physical production of such circuits, which requires expensive and precise machining. Moreover, the realization of complex structures is limited by subtractive manufacturing technologies such as computer numerical control (CNC) and electro discard machining (EDM). Such techniques also cannot be used for the realization of various high-frequency WG circuits in a single piece, which allows for avoiding power losses due to electrical contact issues among different parts [12].

To challenge the above issues additive manufacturing (AM) technologies have been proposed as an alternative for the production of various high-frequency electronic circuits [12], [13], [14], [15]. WG components in such a scheme can be printed out of nonconductive material using, e.g., stereolithography process (SLA) [16], [17], [18], fused filament deposition (FFD) [19], [20], and polyjet printing [21], [22], [23]. Nevertheless, such approaches require an additional fabrication step, during which the 3-D-printed

plastic components are metal coated. An alternative solution is direct 3-D printing out of metallic materials [14] such as stainless steel, aluminum, titanium, nickel, or copper using powder bed fusion (PBF) technologies such as binder jetting (BJ) [24], [25], metal selective laser melting (SLM) [26], [27] and direct metal sintering (DMS) [28], [29]. In the context of RF/microwaves, SLM represents one of the most promising AM techniques, as complex geometries with internal features and channels can be easily realized.

One of the most significant issues related to WG circuit production through SLM technology, in comparison with subtractive technologies, is the high surface roughness [30], [31] on manufactured components. Roughness influences the insertion losses of fabricated circuits, especially visible at higher frequencies [32], [33], [34], [35], [36], [37]. In literature, many solutions for smoothing additively manufactured surfaces are presented, but most of them are used on plastic components [38], [39], [40]. For metal parts, on the other hand, mechanical polishing techniques are commonly used where vibration, tumbling, or rotation action forces the abrasive medium against the surface [41]. With these methods, outer surfaces are easily processed, while inner walls are challenging, especially for parts with fine internal features, since usually, the abrasive medium is too large to fit inside or too aggressive. An alternative is the electropolishing process [41], where the current-assisted reverse plating process in an electrolyte bath is used for smoothing the surface. It is well suited for the discussed application as the liquid could easily penetrate the interior. However, chemicals are required, making the process more expensive.

In this article, a novel low-cost polishing method for metal additively manufactured components is presented. This method is applied to WG components operating in the millimeter frequency range. In this regime, a wall roughness of tens of microns is hardly acceptable. Rough internal surfaces impact the electrical performance of components as it results in lower effective conductivity of walls as compared to bulk value. This is of importance since conductor-related losses are the only source of attenuation within the circuits, while in many cases metal type, composition, or bulk conductivity, is technology specific and cannot be altered to some extent. To overcome the challenge of the abrasive medium efficiently penetrating internals with long channels and/or (multiple) cavities having cross section dimensions in the range sub- to a few millimeters, a rotary tumbler is proposed to be used in combination with micro glass beads. An experimental study is carried out on a set of additively manufactured WG sections and bandpass filters operating within cm- and mm-wave frequency range, produced through SLM technology. Polishing impact on both mechanical and electrical properties was studied, showing surface roughness reduction by 18% and sixth order filter's insertion loss reduction at 23 GHz by 40%, after 24 h of tumbling with 300–400 $\mu$m large microbeads, hence validating the superior performance and applicability of the proposed method.

## II. Additively Manufactured All-Metal WGs

In this section, the conductor and surface properties of additively manufactured all-metal WGs are studied. The impact

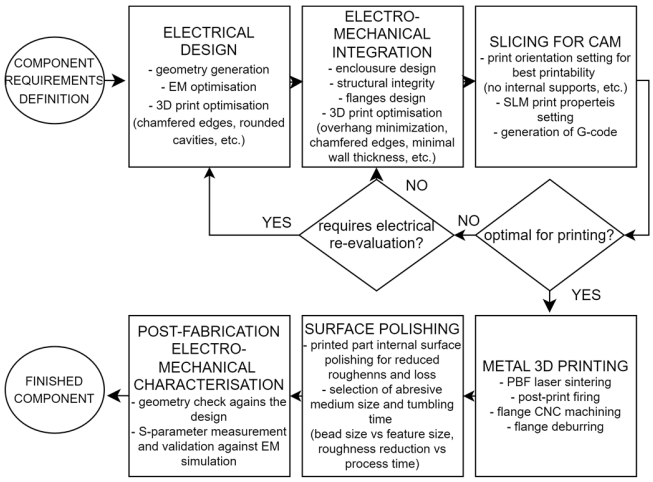


Fig. 1. Flowchart of the design to fabricate the process of microwave components using the proposed approach.

of effective conductivity (influenced by metal conductivity), frequency of operation, and surface roughness on total power loss (TPL) (which is the key electrical performance metric for metal WG circuits), is elaborated. A low-cost surface polishing method for additively manufactured printed WG components postprocessing is introduced. Finally, test vehicles for experimental assessment of the method's performance are developed.

A general flowchart of the employed design to fabricate process is depicted in Fig. 1 where two domains are visible: digital preparation and physical fabrication. First, the component type and related requirements are defined. This is followed by an electrical design where the components' geometry is determined by means of full-wave electromagnetic (EM) simulations and optimization using computer aided desing (CAD) software. At this stage, the geometry optimization may already take advantage of the properties of the intended fabrication technology, i.e., 3-D printing which provides true 3-D flexibility. In addition, features that are helpful for better printability may already be accounted for such as edge chamfering or rounded corners. This is followed by electro-mechanical integration using yet another type of CAD software where mechanical features ensuring structural integrity such as wall thickness, coupling flanges, mounting holes, sub-component integration, and 3-D printing requirements adjustment are done. The next step is file preparation for computer aided manufacturing (CAM) using slicing software. Parameters such as part placement and print orientation are set and the software slices the model into layers and generates the *G*-code for CAM. It provides a report with potential print issues such as print instability, overhands, internal supports, too-thin walls, and so on. If any problem is indicated, either one or two earlier steps must be re-revisited depending on whether mechanical fixes may or may not affect the electrical performance. Otherwise, the part fabrication begins starting with 3-D printing using the SLM technology out of metal powder. Then the part is cut out of the built platform and if necessary, CNC machined to, e.g., flatten/surface flanges. Finally, the proposed post-processing method is applied to reduce the surface roughness

of the print where glass beads are used as a polishing medium to tumble along with the part leading to reduced roughness and thus reduced power losses. The finished part is then characterized in terms of mechanical (geometry accuracy) and electrical (fulfillment of design requirements). If the objectives are fulfilled then the part is ready, if not the data can be fed back to the design loop and corrected for in the next iteration.

### A. Surface Roughness Impact on WG Propagation Characteristics

To investigate the fabrication method's effect on WG components, we first consider wave propagation properties through a section of an air-filled rectangular WG operating in the fundamental $TE_{10}$ mode. Signal transmission through a matched ($S_{11} = S_{22} = 0$) transmission line section is expressed in terms of scattering parameters (S-parameters) as follows:

$$S_{21} = S_{12} = e^{-\gamma l} = e^{-(\alpha + j\beta)l} \tag{1}$$

where $l$ is the physical length of the lines, while $\gamma$ is the complex propagation constant, and $\alpha$ and $\beta$ are, respectively, the attenuation and propagation constants. As provided in [42], the complex propagation constant of the TE10 mode is

$$\gamma = \sqrt{(R' + j\omega L')\left(\frac{1}{R'' + j\omega L''} + G' + j\omega C'\right)} \tag{2}$$

and can be expressed in terms of per- and times-unit-length model resistance $R$ (conductor-related losses), inductance $L$, conductance $G$ (dielectric-related losses), and capacitance $C$. Conductivity and surface roughness of the guide's conductor has a significant impact on parameters representing the interaction of magnetic fields with conductive media, namely $R'$ and $R''$, and partially $L'$ and $L''$. In the case of an ideally smooth surface that represents the abrupt transition from dielectric into conductive media, the skin effect occurs, and thus, the current skin depth can be defined as follows [43]:

$$\delta = \frac{1}{\sqrt{\pi \mu_0 \mu_r \sigma_{dc} f}} \tag{3}$$

where $\mu_0$ and $\mu_r$ are the vacuum and relative permeability, $\sigma_{dc}$ is the conductivity, and $f$ is the frequency. Nevertheless, it needs to be underlined, when the skin depth decreases to a similar range as the variation in surface profile due to roughness (as a reference, skin depth at 30 GHz for copper (60 MS/m) $\approx$ 0.38 $\mu$m, while for stainless steel (1.5 MS/m) $\approx$ 2.38 $\mu$m) [42], then (3) is no longer valid. In such a case, the conductivity is a variable parameter continuously depending on the spatial coordinates. It can be determined using, e.g., the Gradient Model [44] that requires only the rms roughness value $R_q$ if the surface roughness follows the normal distribution. The impact of surface roughness is transferred into effective, frequency-dependent material parameters $\sigma_{\text{eff}}$ (lower than $\sigma_{dc}$), and $\mu_{r,\text{eff}}$ (higher than $\mu_r$). Then, the skin depths in rough surfaces for current densities $\delta_c$ and magnetic fields $\delta_m$ can be derived [42], to finally obtain $R$ and $L$. The ohmic loss $R$ mainly affects the attenuation coefficient, while the inner inductance $L$ is related to the phase coefficient. Moreover, it is necessary to differentiate between the frequency region close to the cutoff frequency $f_c$ and the usually used transmission region of a WG from $1.25 f_c$ to $1.9 f_c$, since rough surfaces affect the propagation properties with different orders of magnitude. On the one hand, the cutoff frequency decreases with increasing $R_q$ due to an increase in both $R$ and $L$, but on the other hand, increasing $R_q$ imposes a severe increase of attenuation constant $\alpha$ in the typical frequency range. When $R_q$ is much higher than the skin depth, $b$ is increased at least twofold [42]. The impact of increased $L$ is especially reflected in the phase coefficient $\beta$ in the frequency region around $f_c$. Like $\alpha$, the responses in $\beta$ also exhibit a shift toward lower frequencies with increasing $R_q$. In addition, the slope reduces during the transition from attenuation to transmission region. However, in the typical frequency range of the WG, $\beta$ is relatively insensitive to variations in $R_q$.

The previous study can be extended to resonators, which are basic building blocks for many circuits such as filters. The quality factor $Q$ of a resonator describes its ability to store energy, and the unloaded quality factor $Q_U$ is the maximum quality factor of the system. When there are only conductor losses, the $Q_U$ value is inversely proportional to $\alpha$ and thus decreases when $R_q$ increases. High $Q_U$ is especially important when high selectivity filters operating at high frequency with low in-band insertion losses IL are to be realized, since [45]

$$\text{IL}(f_0) = 4.343 \frac{N}{Q_U \frac{\Delta f}{f_0}} \tag{4}$$

where $N$ is the filter's order, while $\Delta f / f_0$ and $f_0$ are the fractional bandwidth and midband frequency, respectively. The impact of conductor properties (including surface roughness) becomes more pronounced as the number of resonators increases. The passband of a filter is also affected since $R_q$ affects the propagation constant and in turn the resonant frequency. However, as indicated earlier within the WG's typical frequency range, this impact is relatively low and is more visible for highly selective filters.

In summary, the overall power losses in WG circuits depend on the frequency range of operation, bulk conductivity, surface roughness, and WG geometry. Therefore, it is crucial for a given fabrication technology and material to provide the smoothest inner surfaces where current flows and magnetic fields propagate, to minimize power losses.

### B. Test Vehicles

The analysis presented in Section II-A suggests that two types of circuits might benefit differently from low surface roughness, namely: broadband sections of transmission lines where the attenuation constant is minimized, and narrowband-like filters where the unloaded quality factor is maximized. Therefore, a set of test vehicles was designed to include both types to operate in the cm/mm-wave frequency range.

First, rectangular WGs in various geometries were considered.

1) A 150 mm long straight section in WR-90 geometry (cross section of 22.86 $\times$ 10.16 mm, recommended band between 8.2 and 12.4 GHz).

2) A 100 mm long 90° twisted (five wavelengths) section in WR-42 geometry (cross section of 10.67 × 4.32 mm, recommended band between 18 and 26.5 GHz).

3) A 100 mm long straight section in WR-28 geometry (cross section of 7.11 × 3.56 mm, recommended band between 26.5 and 40 GHz).

Each guide was equipped with a flange for mating with the measurement equipment. On top of loss reduction, the usability of the method for complicated internal walls such as spiraled or rotated ones was benchmarked with the WG twist. Relatively long sections were realized to maximize the $\gamma l$ term change due to attenuation factor change since the measurement of low losses is limited by measurement system uncertainty. The full-wave models were simulated in *Ansys HFSS* software assuming metal properties and surface finish provided in Section II-C (Groisse model for roughness used). The predicted losses are 0.013 dB/cm for WR-90 at $f_{0\_WR-90} = 10.5$ GHz, 0.048 dB/cm for WR-42 at $f_{0\_WR-42} = 22.25$ GHz, and 0.073 dB/cm for WR-28 at $f_{0\_WR-28} = 33.25$ GHz. Considering the EM-calculated losses of the WG, the unloaded quality factor can be established to be ∼328 at $f_{0WR-42}$.

Second, narrowband filters of different orders and bandwidths were developed.

1) A semi 3-D printing optimized second order bandpass filter, namely BPF2_42 in WR-42 geometry operating at the center frequency of 24 GHz with a relative bandwidth of ∼8% for which the (4) yields $IL_{min}$ of 0.265 dB. The minimal dimension of the resonator cavity is ∼5.5 mm; the minimal iris opening is ∼4.4 mm.

2) A fully 3-D printing optimized sixth order bandpass filter, namely BPF6_42 in WR-42 geometry operating at the center frequency of 23 GHz with a relative bandwidth of ∼10% for which the (4) yields $IL_{min}$ of 0.678 dB. The minimal dimension of the resonator cavity is ∼10.6 mm; the minimal iris opening is ∼4.4 mm.

3) A downscaled to WR-28 geometry version of the BPF6_42, namely BPF6_28 operating at the center frequency of 38 GHz. The minimal dimension of the resonator cavity is ∼5.6 mm, while the minimal iris opening is ∼3 mm.

Advanced layout optimization for AM [27], [46] was applied within a dedicated tool in *InventSim* software [47]. The final layout of both filters is provided in Fig. 2. BPF2 has a filter length of 20.6 mm, BPF6_42 of 73.3 mm, and BPF_28 of 39 mm. Adding the WG sections, the overall component length sums up to 50, 100, and 100 mm, respectively.

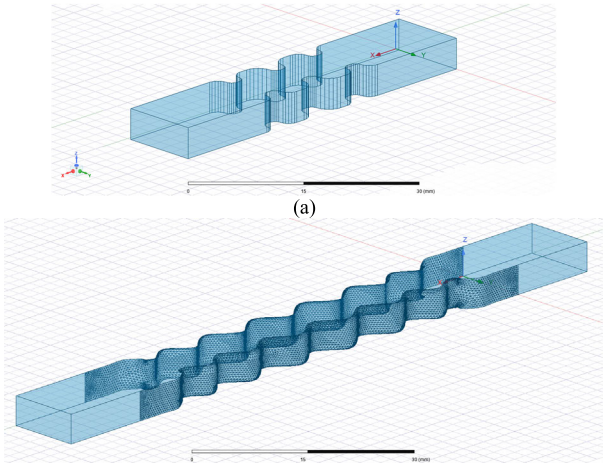

Fig. 2. Layout of the developed (a) second and (b) sixth order bandpass filters in WR-42 geometry featuring 3-D printing optimized geometry.

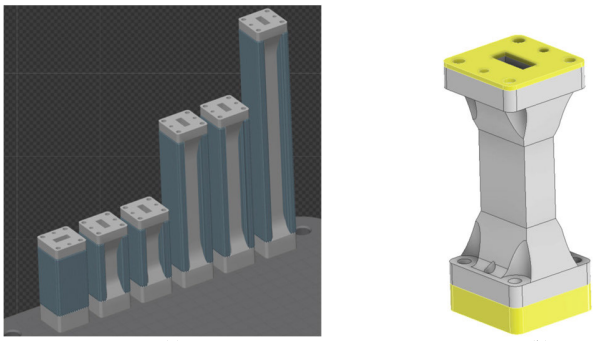

Fig. 3. Test vehicle orientation on the print bed with supports added (a) is set in the slicing software. Exemplary test vehicle view where yellow color indicates stock in the flange region that is removed and machined with CNC after detachment from building plate (b).

### C. AM Process

In PBF, the physical and chemical properties of powder particles affect the final quality of additively manufactured components [48]. Fine particles enable high-density parts with good surface quality, while the spherical shape improves flowability and, as a result, mechanical properties. Irregular powder particles can lead to poor surface finish, low density, and increased defects.

In this article, PBF based on SM was adopted, namely the printer [49] was used to 3-D print the test vehicles out of Stainless Steel 316L [50]. The average surface roughness ($R_a$) of SS316L additively manufactured components is commonly 11 ± 2 $\mu$m (JIS B 0601-2001 -ISO 97) after bead blasting (assuming Gaussian probability density function (PDF) $R_q = 1.25$, $R_a = 13.75 \pm 2.5$ $\mu$m). All test vehicles (having a general form of a long rectangular tube) were oriented on the building plate with flanges parallel to the print bed as shown in Fig. 3. Such orientation results in support only on the outside of the WG to carry the load of the top flange contour, while there are no supports inside the WG cross section. Each printed test piece has the same surface finish with the same lay, i.e., parallel deposited metal layers oriented perpendicular to the direction of wave propagation. Finally, to reduce the number of variables affecting the measured power losses, both flanges were CNC-milled postfabrication so that very good electrical contact is ensured between the measurement instrument's WG flanges and device-under test WG flanges. The fabricated test vehicle set is presented in Fig. 4.

### D. Surface Polishing

Additively manufactured metal parts usually have a poor surface finish in comparison to milled and turned components. Many post-processing techniques can ensure that additively manufactured metal parts meet dimensional requirements, performance characteristics, and even esthetic

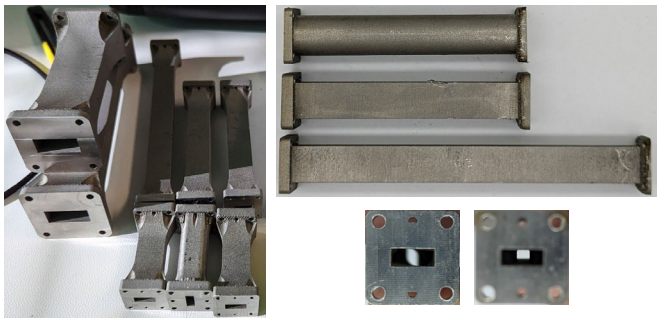

Fig. 4. Photographs of the fabricated test vehicles.

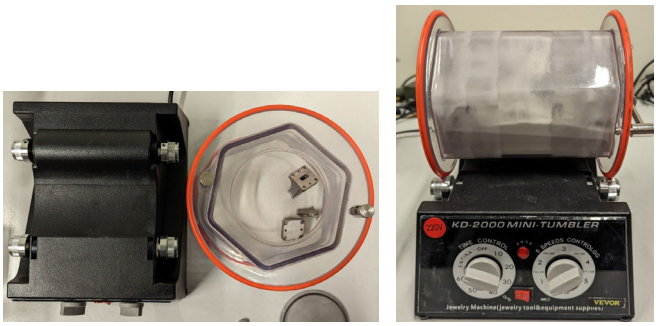


(a) (b)

Fig. 5. Photograph of the setup used for polishing of parts. (a) Barrel loaded with glass microbeads. (b) Running machine during polishing cycle.

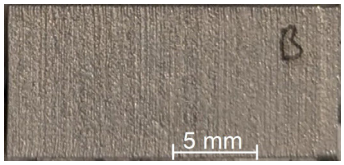


Fig. 6. Photograph of the fabricated sample for mechanical properties analysis. Layers orientation is clearly visible and thus the resulting roughness is orientation dependent. The sample area equals 20 × 10 mm.

guidelines. These processes include green sanding, media blasting, tumble finishing, pin finishing, vibratory finishing, and electropolishing. The WG components present internal channels, therefore, one of the most promising surface post-processing treatments is electropolishing [51], sometimes referred to as "reverse plating" as it utilizes a phosphoric-based electrolyte bath and rectified current to remove surface material. Electropolishing eliminates micro-peaks (high points within the microscopic surface) to reduce surface roughness to a higher level of smoothness than other finishing methods. Moreover, the electropolishing solution can reach every part of the component surface. This can include internal gaps and cavities that other finishing methods cannot reach. A smoother surface means fewer places for corrosive elements to take hold and thus extend part lifetime. Finally, electropolishing generally delivers a more consistent finish across the entire part surface. In contrast to that, many other polishing systems can leave marks or patterns on the surface. A large drawback of the method is its relatively high cost and careful handling as chemical bath is needed.

In this study, a mechanical barrel-based surface polishing method is introduced and validated. This method presents the advantages of electropolishing in combination with microbead-blasting Barrel polishing [41] is a surface-improving operation in which a mixture of parts, media, and compounds are placed in a six- or eight-sided barrel and rotated at a predetermined speed to round corners, deburr, grinding, descaling, deflashing, improving surface finish, burnishing, polishing, and radiusing parts in bulk. Tumbling parts are placed in a rotating barrel, and an abrasive media is introduced inside the barrel. Producing good surface finishes depends on the right selection of tumblers, abrasives, lubricating agents, carrying agents, and polishing agents. Very little handling is required for the process and many metal parts can be processed at once while the process can be finished in a tumbling barrel overnight, or in an hour or less in a high-energy machine. Barrel speeds in dry tumbling are generally kept at 28–32 r/min. On the other hand, in the microbead-blasting process, a very fine abrasive media and a miniature nozzle are used to produce a controllable abrasive jet that can target and remove microns of material. The result is a reliable and repeatable method for deburring, texturing, cleaning, stripping, etching, or milling part surfaces. The abrasive medium is easily available in a gamut in hardness (from soft compounds like sodium bicarbonate to hard ceramics like silicon carbide), that suits different materials to be processed as well in different shapes from spherical to blocky or pointy and sizes ranging from a couple of microns to hundreds of microns. Despite advantages, the process itself uses a directed jet of medium and thus internal cavities and channels of additive manufactured components parts cannot be reached.

In this study, the dry tumbling method using the Vevor KD-2000 jewelry grade mini rotary tumbler (5 kg max load, 4.5 l barrel dimensions of 190 × 180 mm, opening diameter of 90 cm), in combination with 300–400 $\mu$m large glass microbeads was employed. Such a combination ensures that the container size is large enough to fit a few parts while the medium size is small enough to easily penetrate the insides of the parts even having openings in the range of single millimeters. Glass microbeads are well suited for processing stainless steel and due to their structure leave the surface a bit satin, uniform, and smooth. The larger the beads the more effective they are and shinier, hence smoother, the surface. For example, 40–70 $\mu$m leads to a matte finish whereas 300–400 $\mu$m returns very shiny surfaces. On the other hand, too-large beads will not penetrate chambers with small openings and will not affect areas in proximity to sharp corners. An additional benefit of using microbeads in the dry tumbling process is that they provide an extraordinary amount of surface area to carry the dirty residue, thus avoiding having the residue embedded into the surface of the parts. A photograph of the polishing setup is presented in Fig. 5. The tumbler is filled with beads up to roughly three quarters of its volume.

## III. Experimental Results

The proposed surface polishing method was experimentally validated within the postprocessing of test vehicles (broadband and resonant ones) operating within the cm/mm-wave frequency range. The impact of polishing on the resulting mechanical and electrical properties of circuits is provided and discussed in detail. Each test vehicle was measured before

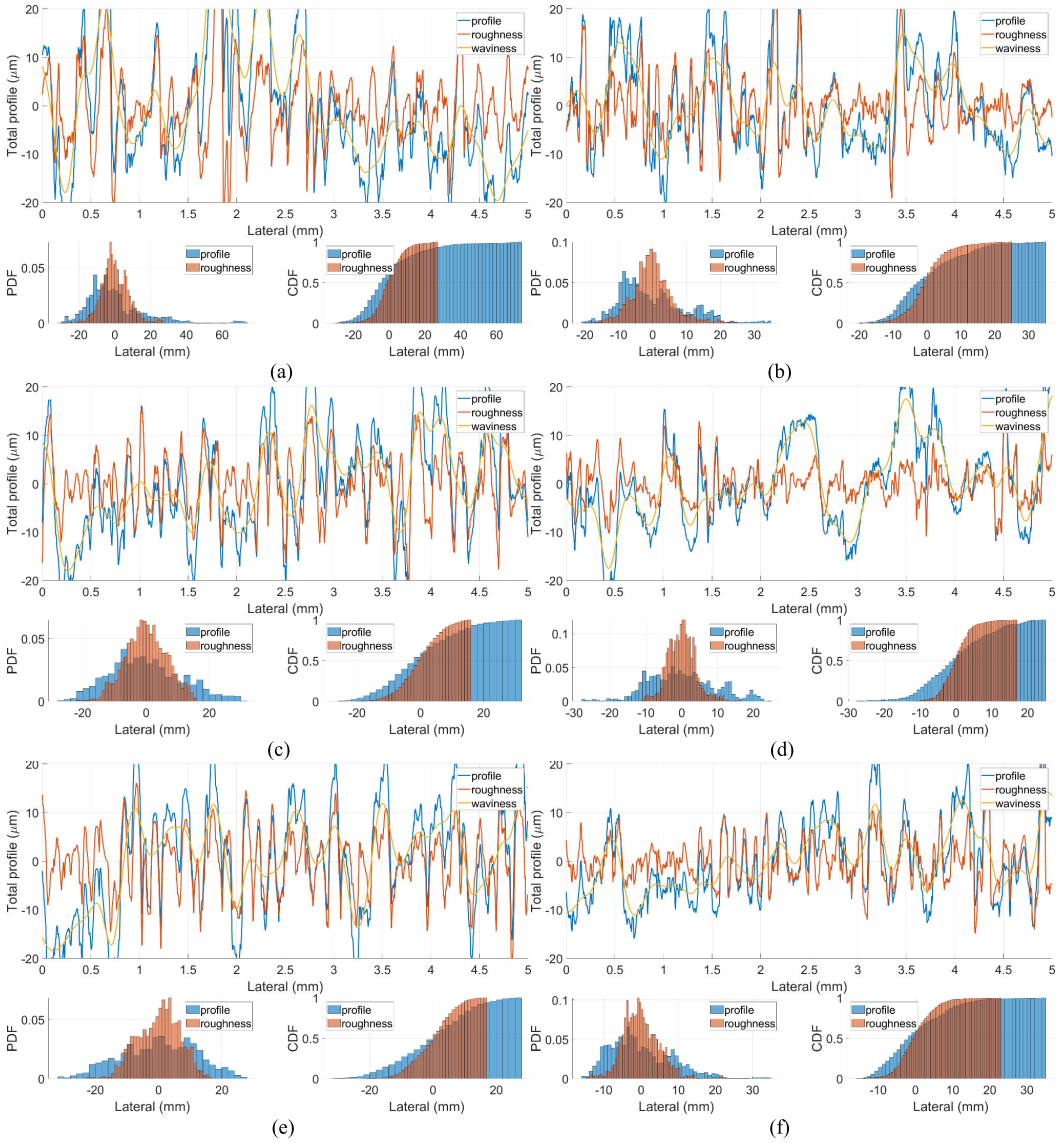


Fig. 7. Measured surface profiles of the printed specimen. (a) and (b) No polishing applied, (c) and (d) after 24 h of polishing, and (e) and (f) after 48 h of polishing. Profiles at orthogonal directions (orientation parallel (a), (c), and (e) and perpendicular (b), (d), and (f) to layer arrangement).

polishing and then after one and two cycles of polishing. Each 24-h (12-h) polishing cycle was carried out at 50 rotation-per-minute speed (to avoid microbeads sticking to internal surfaces due to centrifugal force instead of tumbling).

### A. Mechanical Performance

First, the mechanical properties of additively manufactured test vehicles were assessed. Dimensions of the parts shown in Fig. 4 were measured using a digital caliper (10 $\mu$m least significant digit) in two different spots and averaged to assess the fabrication tolerance including post-heat treatment shrinkage. The results are summarized in Table I: the internal cross section of WG components shrunk after all processing steps. Dimension reduction is in the range of 1%–3%.

In the next step, the Bruker Dektak XT stylus profilometer was used to evaluate surface roughness: 1) before polishing; 2) after 24 h of polishing; and 3) after 48 h of polishing. Two parameters were used for comparison purposes, i.e., rms roughness value $R_q$ and the average surface roughness $R_a$. Since the internal surface profile of test vehicles could not be nondestructively measured between tumbling cycles, a dedicated 20 × 10 × 3 mm specimen shown in Fig. 6 was fabricated and processed in the same way. At every step, an optical inspection was carried out as well, and a 5 mm long surface profile was captured in two orthogonal directions. The resulting roughness and waviness profiles are provided in Fig. 7, the optical images are shown in Fig. 8, while the average and rms roughness values are summarized in Table II.

TABLE I
MEASURED DIMENSIONS OF THE FABRICATED PROTOTYPES AND CALCULATED DEVIATION Δ FROM THE DESIGN VALUES

| | $a$ (mm) | $\Delta a$ | $b$ (mm) | $\Delta b$ |
|---|---|---|---|---|
| **WR-90 section** | 22.68 | -0.8% | 10.07 | -0.9% |
| **WR-42 twist** | 10.59 | -0.8% | 4.23 | -2.2% |
| **WR-28 section** | 6.99 | -1.8% | 3.43 | -3.7% |
| **WR-42 BPF2_42** | 10.61 | -0.6% | 4.24 | -2.0% |
| **WR-42 BPF6_42** | 10.60 | -0.7% | 4.24 | -2.0% |
| **WR-28 BPF6_28** | 7.01 | -1.5% | 3.45 | -3.2% |

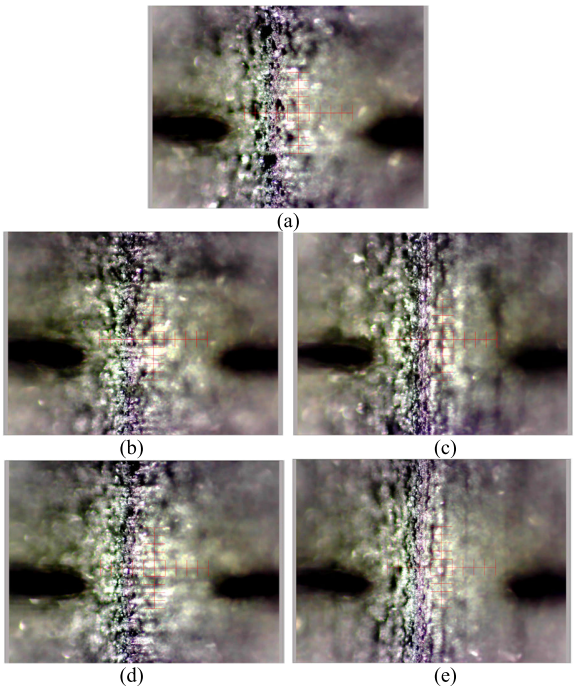


Fig. 8. Optical image of the printed specimen's surface. (a) No polishing applied, (b) and (c) after 24 h, and (d) and (e) after 48 h of polishing. The total picture width and height is 2.25 mm (1× zoom). Photographs at orthogonal directions [(b) and (d) orientation parallel and (c) and (e) perpendicular to layer arrangement]. The layered print pattern is clearly visible.

TABLE II
ESTABLISHED ROUGHNESS OF THE SLM PRINTED SPECIMEN FROM A 5 MM LONG PATH IN TWO ORTHOGONAL DIRECTIONS

| **Orientation** | perpendicular to layer arrangement | | | |
|---|---|---|---|---|
| **Profile** | primary | | roughness | |
| **Metrics** | $R_a$ (µm) | $R_q$ (µm) | $R_a$ (µm) | $R_q$ (µm) |
| **Prior polishing** | 12.05 | 16.63 | 6.00 | 7.85 |
| **After 24h** | 9.23 | 11.38 | 5.19 | 6.47 |
| **Improvement** | 23.4% | 31.6% | 13.5% | 17.6% |
| **After 48h** | 9.73 | 11.82 | 5.37 | 6.58 |
| **Improvement** | - | - | - | - |
| **Orientation** | parallel to layer arrangement | | | |
| **Profile** | primary | | roughness | |
| **Metrics** | $R_a$ (µm) | $R_q$ (µm) | $R_a$ (µm) | $R_q$ (µm) |
| **Prior polishing** | 8.07 | 9.99 | 4.48 | 6.12 |
| **After 24h** | 7.60 | 9.46 | 2.99 | 3.87 |
| **Improvement** | 5.8% | 5.3% | 33.3% | 36.8% |
| **After 48h** | 6.83 | 8.45 | 3.81 | 4.95 |
| **Improvement** | - | - | - | - |

Both the optical and the surface analysis reveal the typical characteristics of part made by SM: irregularities, larger melted grain clusters, and relatively large waviness. The collected profiles must be considered random and as just a local representation of the surface. Nevertheless, they allow us to assess the polishing technique performance to a certain degree.

The highest roughness is found in the planes parallel to the printing plate, while along the direction orthogonal to the printing plate a lower roughness is observed. In both directions, the PDF for roughness is close to the Gaussian distribution. Finally, it is clearly seen that the specimen surface is smoother after 24 h of polishing while an extra 24 h makes no significant difference. Roughness $R_q$ reduction by 17% and 37% are obtained for orientations perpendicular and parallel to layer arrangement, respectively. Considering the above, various polishing times were applied to the fabricated WG demonstrators for a better assessment of polishing time versus loss reduction assessment.

TABLE III
MEASURED IMPACT OF POLISHING ON WG ATTENUATION CONSTANT (EXPRESSED THROUGH TPL METRICS). POSITIVE DIFFERENCE Δ MEANS VALUE REDUCTION WITH RESPECT TO THE BASE ONE

| | | $\alpha$ @ $f_0$ (dB) | $\Delta\alpha$ (%) | $\alpha$ @ $f_0$ (dB/cm) |
|---|---|---|---|---|
| **WR-90** | Pre | 0.186 | | 0.0124 |
| | After 24h | 0.164 | 11.9 | 0.0109 |
| | After 48h | 0.195 | -2.9 | 0.0130 |
| **WR-42 twisted** | Pre | 0.615 | | 0.0615 |
| | After 12h | 0.506 | 17.7 | 0.0506 |
| | After 24h | 0.499 | 19.0 | 0.0490 |
| **WR-28** | Pre | 0.475 | | 0.0475 |
| | After 12h | 0.450 | 5.2 | 0.0450 |
| | After 24h | 0.430 | 9.5 | 0.0430 |

TABLE IV
MEASURED IMPACT OF POLISHING ON BANDPASS FILTER IN-BAND INSERTION LOSS AND EXTRACTED UNLOADED QUALITY FACTOR. POSITIVE DIFFERENCE Δ MEANS VALUE IMPROVEMENT WITH RESPECT TO PRE-POLISHING

| | | $f_0$ (GHz) | $BW$ (GHz) | $IL$ @ $f_0$ (dB) | $\Delta IL$ @ $f_0$ (%) | $Q_U$ @ $f_0$ (Eq. 4) | $\Delta Q_U$ (%) |
|---|---|---|---|---|---|---|---|
| **BPF2_42** | EM | 23.93 | 1.95 | | | | |
| | Pre | 24.8 | 1.69 | 0.67 | | 190.2 | |
| | 24h | | | 0.65 | 9.5 | 196.1 | 3.1 |
| | 48h | | | 0.62 | 15.4 | 205.6 | 8.1 |
| **BPF6_42** | EM | 23.05 | 2.4 | | | | |
| | Pre | 22.97 | 2.07 | 2.02 | | 142.8 | |
| | 24h | | | 1.27 | 39.7 | 227.4 | 59.2 |
| | 48h | | | 1.24 | 38.3 | 233.7 | 63.6 |
| **BPF6_28** | EM | 38.13 | 4.35 | | | | |
| | Pre | 38.46 | 4.04 | 1.42 | | 160.8 | |
| | 12h | | | 1.27 | 10.5 | 195.3 | 21.4 |
| | 24h | | | 1.2 | 15.5 | 207.2 | 28.8 |

### B. Electrical Performance

Finally, the electrical properties of the additively manufactured test vehicles were assessed. The dc conductivity of the specimen was measured using the Hioki 3522-50 LCR meter to be 0.96 MS/m which is 71% of the bulk value for the SS316L. This was followed by measuring the scattering parameters of the test vehicles using the Agilent PNA N5224A vector network analyzer at an IF bandwidth of 1 kHz. The calibrated reference plane is set at the WG flange, using WR-90, WR-42, and WR-28 Thru-Reflect-Line cal-kits. Measurements were taken before polishing, and once after each 24 h (12 h) polishing run. Since very low loss differences were to be measured, the $S_{21}$ measurement uncertainty of the VNA being 0.02 dB [52] cannot be overlooked, and thus a strict protocol was followed. To ensure repeatable results, each time all the screws that force mating the WG flanges were tightened with the same torque force. Moreover, after calibration, the cables connecting VNA with the coax-to-WG adapters were kept in the same position. The measured frequency response of the pre-polished circuits is provided for the WG section in Fig. 9, while for bandpass filters in

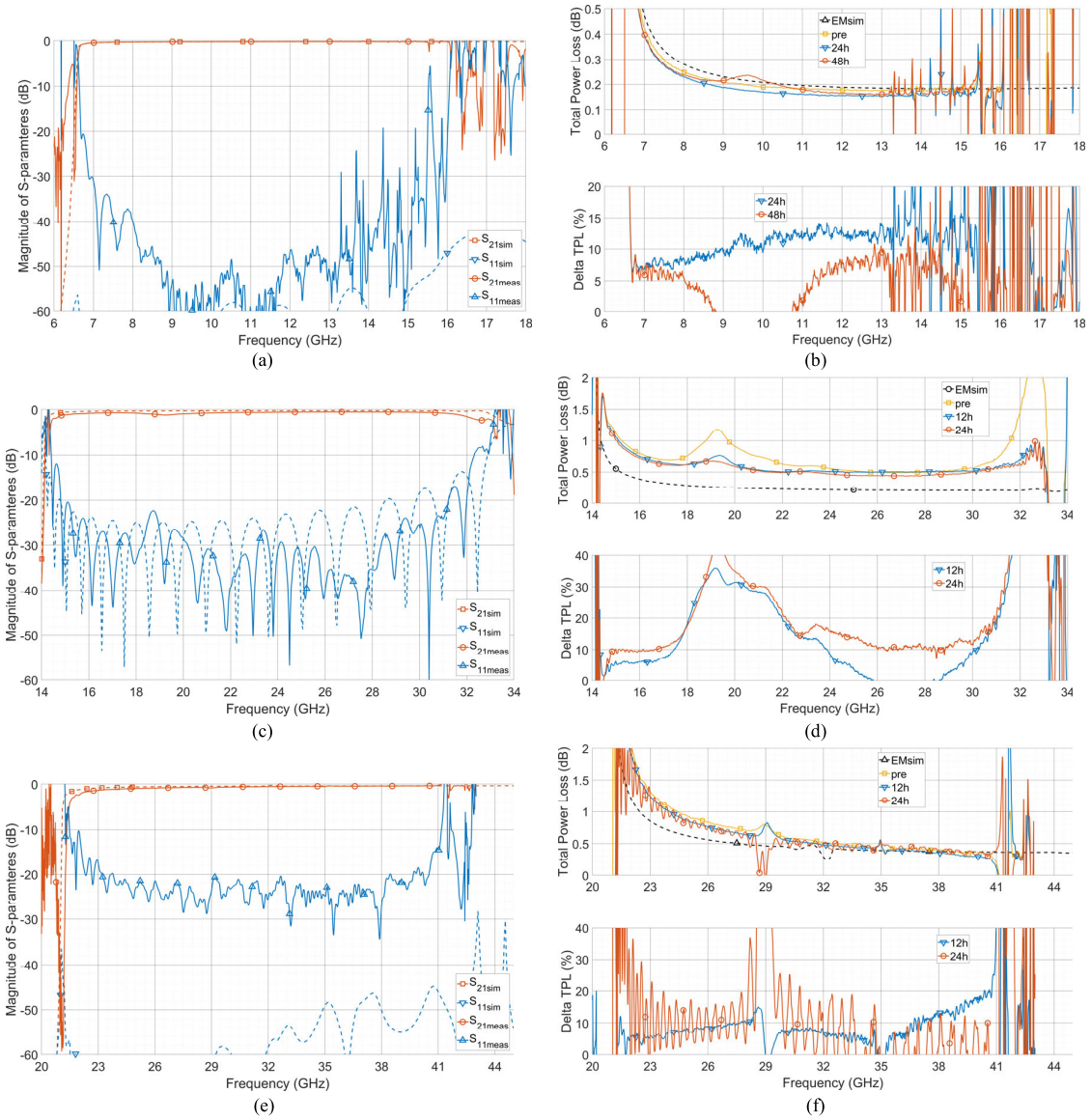


Fig. 9. Measured (solid lines) pre-polishing S-parameters of the SLM-fabricated (a) WR-90, twisted (c) WR-42, and (e) WR-28 sized WG sections along with EM simulated ones overlayed (dashed lines). Measured impact of polishing on TPL of (b) WR-90, (d) WR-42, and twisted (f) WR-28 sized WG sections: pre-polishing, after one and two rounds of polishing. Delta TPL referenced to pre-polishing TPL.

Fig. 10. Moreover, the attenuation constant expressed through the TPL is defined as $\text{TPL} = 1 - \left(|S_{21}|^2 + |S_{11}|^2\right)$ for both WG sections and BPFs is confronted with the full-wave simulated EM to assess the polishing effectiveness on the power loss. Finally, the percentage improvement after each round of polishing is determined. The results are also summarized in Table III for WGs and in Table IV for BPFs. From the above results, the following conclusions can be drawn. First, the VNA measurement uncertainty has a visible impact on the experimental results which manifests itself in, e.g., erroneous percentage improvement as the in-process TPL values are relatively small. Second, it is seen that a slight dimension reduction is observed due to metal printed part shrinkage. This can be easily counteracted by slightly scaling up the model before printing. Third, for the proposed process, the polishing time is selected as a tradeoff between potential roughness reduction and the time required. It is seen that even after only 12 h of polishing a dozen percent improvement is seen with longer times the gain being less and less significant. Fourth, glass bead size must be selected considering feature size since the medium must freely penetrate cavities.

The difference is seen, e.g., between loss improvement for WR-42 geometry (even in a twist configuration) versus WR-28. In addition, in BPF6_28 the minimal iris is only an order of magnitude larger than the bead radius. For higher bands smaller beads (e.g., 150–200 $\mu$m radius) could yield better results. Fifth, since a rough surface is inevitably bounded by the fabrication technique, the use of different base materials such as aluminum (roughly 30 times better conductivity) powder in combination with the proposed post-processing method would provide a very low loss metal 3-D printed mm-wave components.

Finally, results obtained in this study for narrowband filters were compared with the state-of-the-art. A summary is provided in Table V from which it can be noted that the

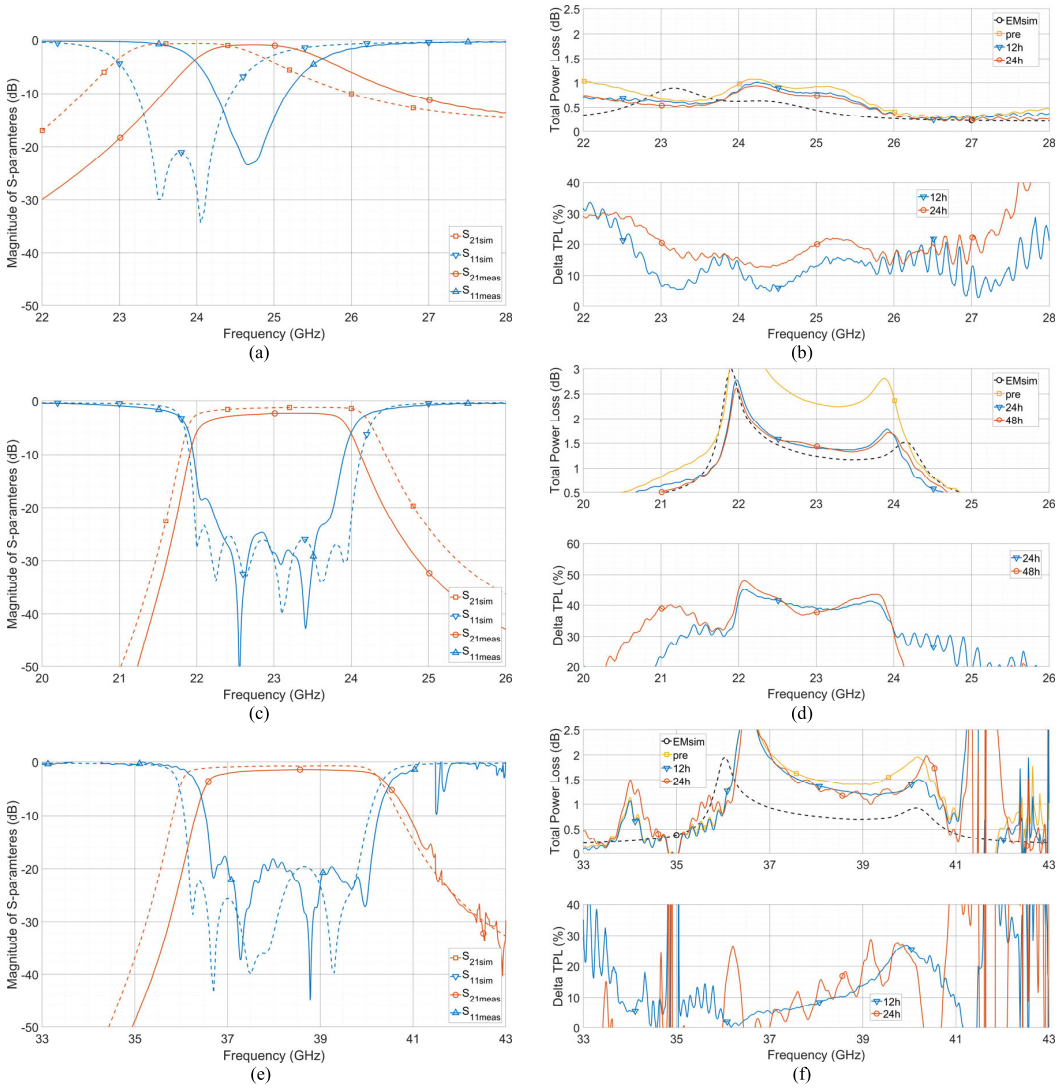


Fig. 10. Measured (solid lines) pre-polishing S-parameters of the SLM-fabricated (a) BPF2_42, (c) BPF6_42, and (e) BPF6_28 filters along with EM simulated ones overlayed (dashed lines). Measured impact of polishing on TPL of (b) BPF2_42, (d) BPF6_42, and (f) BPF6_28 sized WG sections: pre-polishing, after one and two rounds of polishing.

TABLE V

STATE-OF-THE-ART ADDITIVELY MANUFACTURED FILTERS VERSUS PROPOSED FABRICATION SCHEME

| | Filter Order/Geometry | 3D Technology | $f_0$ (GHz) | BW (%) | $IL$ @ $f_0$ (dB) |
|---|---|---|---|---|---|
| [52] | 4th -order filter/groove gap waveguide | PolyJet electroplated | 35.65 | 1.4 | ~0.5 |
| [53] | 5th -order filter/ rectangular waveguide cavities | SLA# copper plated | 87.5 | 11.5 | ~0.5 |
| [54] | 9th-order filter with shaped resonators | SLM Scalmalloy | ~12 | ~5 | ~1.3 |
| [55] | 5th-order H-plane filter with irises | MLS* stainless steel | 88 | 12 | ~2 |
| This | 6th-order filter with shaped resonators | Polished SLM stainless steel | 23 | 9 | ~1.2 |
| This | 6th-order filter with shaped resonators | polished SLM stainless steel | 38.45 | 10.5 | ~1.2 |

#SLA – Stereolitography, *MLS – Micro Laser Sintering.

proposed fabrication and processing approach provides a very good insertion loss performance even when using a relatively low conductivity metal.

## IV. CONCLUSION

A low-cost polishing method dedicated to all-at-once fabricated WG circuits that employ mechanical barrel tumbling of metal additively manufactured parts, using glass microbeads as an abrasive medium, was introduced, and experimentally validated. In contrast to electropolishing, neither chemicals nor sophisticated equipment is necessary, while similar benefits of good internal cavities and channel penetration and polishing are still provided. A set of test vehicles was fabricated in SS316L using the SLM technique. Both mechanical and electrical properties were assessed before polishing and after one and two polishing rounds. In practice, electropolishing reduces a part's $R_a$ by 10%–30% depending on the starting finish. In the case of the proposed method, improvement is in the range of 6%–23% in terms of surface finish and 14%–33% in terms of roughness. The proposed method's results are comparable to those of industry-standard high-cost high-performance techniques. The obtained results translate into a 10%–20% loss reduction within tested WG geometries and finally between 10% and 40% loss reduction for the tested

second- and sixth-order filters. Therefore, the experimental results certified the performance and applicability of the proposed metal 3-D printed WG components post-processing method that the AM technology is well suited for cm- and mm-wave component fabrication.

## ACKNOWLEDGMENT

Jakub Sorocki and Ilona Piekarz would like to thank Dr. Andrzej Samulak, Independent Researcher, Weilheim in Oberbayern, Germany, for the discussions and invaluable suggestions he provided regarding microwave loss analysis along with the assistance in $X$-band filter design. The authors would also like to thank Dr. Marcin Marzec, Academic Center for Materials and Nanotechnology, AGH University of Science and Technology, Krakow, Poland, for making the profilometer available for surface profile measurements.

## REFERENCES

[1] J. Tsutsumi, M. Seth, A. S. Morris III, R. B. Staszewski, and G. Hueber, "Cost-efficient, high-volume transmission: Advanced transmission design and architecture of next generation RF modems and front-ends," *IEEE Microw. Mag.*, vol. 16, no. 7, pp. 26–45, Aug. 2015.

[2] X. He et al., "Additively manufactured 'smart' RF/mm-wave packaging structures: A quantum leap for on-demand customizable integrated 5G and Internet of Things modules," *IEEE Microw. Mag.*, vol. 23, no. 8, pp. 94–106, Aug. 2022.

[3] G. Macchiarella, G. G. Gentili, N. Delmonte, L. Silvestri, and M. Bozzi, "Design of inline waveguide filters with frequency-variant couplings producing transmission zeros," *IEEE Trans. Microw. Theory Techn.*, vol. 69, no. 8, pp. 3746–3758, Aug. 2021.

[4] M. R. Jiao, F. Zhu, P. Chu, W. Yu, and G. Q. Luo, "Compact hybrid bandpass filters using substrate-integrated waveguide and stripline resonators," *IEEE Trans. Microw. Theory Techn.*, vol. 72, no. 1, pp. 391–400, Jan. 2023.

[5] J. Sorocki, K. Staszek, I. Piekarz, K. Wincza, and S. Gruszczynski, "Directional couplers with reduced coupling requirements as connection of coupled-line sections and left-handed transmission lines," *IET Microw., Antennas Propag.*, vol. 8, no. 8, pp. 580–588, Jun. 2014.

[6] Q. Sun, Y.-L. Ban, X.-F. Li, J.-W. Lian, J. Hu, and Z. Nie, "Multimode CRLH SIW transmission lines for wideband multiport directional couplers and miniaturized beamforming networks," *IEEE Trans. Microw. Theory Techn.*, vol. 71, no. 7, pp. 2828–2841, Feb. 2023.

[7] J. Sorocki, I. Piekarz, K. Janisz, S. Gruszczynski, and K. Wincza, "Frequency multiplexer with improved selectivity using asymmetric response directional filters," *IEEE Microw. Wireless Compon. Lett.*, vol. 28, no. 6, pp. 491–493, Jun. 2018.

[8] M. Wang et al., "Frequency division multiplexer with directional filters in multilayer LCP films at–and -band," *IEEE Microw. Wireless Compon. Lett.*, vol. 32, no. 11, pp. 1287–1290, Nov. 2022.

[9] H.-Y. Xie, B. Wu, Y.-L. Wang, C. Fan, J.-Z. Chen, and T. Su, "Wideband SIW filtering antenna with controllable radiation nulls using dual-mode cavities," *IEEE Antennas Wireless Propag. Lett.*, vol. 20, no. 9, pp. 1799–1803, Sep. 2021.

[10] R. R. Mansour, "Filter technologies for wireless base stations," *IEEE Microw. Mag.*, vol. 5, no. 1, pp. 68–74, Mar. 2004.

[11] J. Cho et al., "Effective size reduction of the metallic waveguide bandpass filter with metamaterial resonators and its 3D-printed version," *Sensors*, vol. 23, no. 3, p. 1173, Jan. 2023.

[12] P. Sanchez-Olivares et al., "Manufacturing guidelines for W-band full-metal waveguide devices: Selecting the most appropriate technology," *IEEE Antennas Propag. Mag.*, vol. 65, no. 2, pp. 48–62, Apr. 2023.

[13] R. Sorrentino and O. A. Peverini, "Additive manufacturing: A key enabling technology for next-generation microwave and millimeter-wave systems [point of view]," *Proc. IEEE*, vol. 104, no. 7, pp. 1362–1366, Jul. 2016.

[14] A. Tamayo-Dominguez, J. Fernandez-Gonzalez, and M. Sierra-Perez, "Metal-coated 3D-printed waveguide devices for mm-wave applications [application notes]," *IEEE Microw. Mag.*, vol. 20, no. 9, pp. 18–31, Sep. 2019.

[15] C. Tomassoni, O. A. Peverini, G. Venanzoni, G. Addamo, F. Paonessa, and G. Virone, "3D printing of microwave and millimeter-wave filters: Additive manufacturing technologies applied in the development of high-performance filters with novel topologies," *IEEE Microw. Mag.*, vol. 21, no. 6, pp. 24–45, Jun. 2020.

[16] A. Tamayo-Dominguez, J.-M. Fernandez-Gonzalez, and M. Sierra-Perez, "Groove gap waveguide in 3-D printed technology for low loss, weight, and cost distribution networks," *IEEE Trans. Microw. Theory Techn.*, vol. 65, no. 11, pp. 4138–4147, Nov. 2017.

[17] J. S. Silva, M. García-Vigueras, T. Debogovic, J. R. Costa, C. A. Fernandes, and J. R. Mosig, "Stereolithography-based antennas for satellite communications in Ka-band," *Proc. IEEE*, vol. 105, no. 4, pp. 655–667, Apr. 2017.

[18] J. Sorocki et al., "Additively fabricated air-filled waveguide integrated with printed circuit board using a through-patch transition," *IEEE Microw. Wireless Compon. Lett.*, vol. 31, no. 11, pp. 1207–1210, Nov. 2021.

[19] M. D'Auria et al., "3-D printed metal-pipe rectangular waveguides," *IEEE Trans. Compon., Packag., Manuf. Technol.*, vol. 5, no. 9, pp. 1339–1349, Sep. 2015.

[20] H. García-Martínez, G. Torregrosa-Penalva, E. Àvila-Navarro, N. Delmonte, L. Silvestri, and M. Bozzi, "3D-printed electromagnetic band-gap band-pass filter based on empty single-ridge waveguide," *IEEE Access*, vol. 10, pp. 53954–53962, 2022.

[21] E. Laplanche et al., "Additive manufacturing of low cost and efficient proof of concepts for microwave passive components," *IET Microw., Antennas Propag.*, vol. 11, no. 14, pp. 1997–2004, Nov. 2017.

[22] E. Lopez-Oliver et al., "3-D-printed compact bandpass filters based on conical posts," *IEEE Trans. Microw. Theory Techn.*, vol. 69, no. 1, pp. 616–628, Jan. 2021.

[23] I. Piekarz et al., "Wideband microstrip to 3-D-printed air-filled waveguide transition using a radiation probe," *IEEE Microw. Wireless Compon. Lett.*, vol. 32, no. 10, pp. 1179–1182, Oct. 2022.

[24] G.-L. Huang, S.-G. Zhou, and T. Yuan, "Development of a wideband and high-efficiency waveguide-based compact antenna radiator with binder-jetting technique," *IEEE Trans. Compon., Packag., Manuf. Technol.*, vol. 7, no. 2, pp. 254–260, Feb. 2017.

[25] E. A. Rojas-Nastrucci, J. T. Nussbaum, N. B. Crane, and T. M. Weller, "Ka-band characterization of binder jetting for 3-D printing of metallic rectangular waveguide circuits and antennas," *IEEE Trans. Microw. Theory Techn.*, vol. 65, no. 9, pp. 3099–3108, Sep. 2017.

[26] B. Zhang et al., "Metallic 3-D printed antennas for millimeter- and submillimeter wave applications," *IEEE Trans. THz Sci. Technol.*, vol. 6, no. 4, pp. 592–600, Jul. 2016.

[27] M. Baranowski, Ł. Balewski, A. Lamecki, M. Mrozowski, and J. Galdeano, "The design of cavity resonators and microwave filters applying shape deformation techniques," *IEEE Trans. Microw. Theory Techn.*, vol. 71, no. 7, pp. 3065–3074, Jul. 2023.

[28] S. Verploegh, M. Coffey, E. Grossman, and Z. Popovic, "Properties of 50–110-GHz waveguide components fabricated by metal additive manufacturing," *IEEE Trans. Microw. Theory Techn.*, vol. 65, no. 12, pp. 5144–5153, Dec. 2017.

[29] S. Manafi, M. Al-Tarifi, and D. S. Filipovic, "45–110 GHz quad-ridge horn with stable gain and symmetric beam," *IEEE Trans. Antennas Propag.*, vol. 65, no. 9, pp. 4858–4863, Sep. 2017.

[30] V. V. P. Babu and V. K. Gb, "A review on 3D printing process on metals and their surface roughness and dimensional accuracy," *Mater. Today, Proc.*, vol. 64, no. 1, pp. 523–530, 2022.

[31] A. P. Golhin, R. Tonello, J. R. Frisvad, S. Grammatikos, and A. Strandlie, "Surface roughness of as-printed polymers: A comprehensive review," *Int. J. Adv. Manuf. Technol.*, vol. 127, nos. 3–4, pp. 987–1043, May 2023.

[32] V. Kyovtorov, I. Georgiev, S. Margenov, D. Stoychev, F. Oliveri, and D. Tarchi, "New antenna design approach—3D polymer printing and metallization. Experimental test at 14–18 GHz," *AEU Int. J. Electron. Commun.*, vol. 73, pp. 119–128, Mar. 2017.

[33] M. Hollenbeck, K. Wamick, C. Cathey, J. Opra, and R. Smith, "Selective laser melting aluminum waveguide attenuation at K-band," in *IEEE MTT-S Int. Microw. Symp. Dig.*, Honololu, HI, USA, Jun. 2017, pp. 45–47.

[34] M. M. Honari, R. Mirzavand, H. Saghlatoon, and P. Mousavi, "Investigation of the 3D printing roughness effect on the performance of a dielectric rod antenna," *IEEE Antennas Wireless Propag. Lett.*, vol. 17, pp. 2075–2079, 2018.

[35] J. Romeu, S. Blanch, N. Vidal, J. M. Lopez-Villegas, and A. Aguasca, "Assessment of 3-D printing technologies for millimeter-wave reflectors," *IEEE Antennas Wireless Propag. Lett.*, vol. 17, no. 11, pp. 2061–2064, Nov. 2018.

[36] J. Sorocki and I. Piekarz, "Low-cost microwave Components' fabrication in hybrid technology of laminates and additive manufacturing on an example of miniaturized suspended directional coupler," *IEEE Access*, vol. 8, pp. 128766–128775, 2020.

[37] M. Almeshehe et al., "Surface roughness impact on the performance of the 3D metal printed waveguide coupler at millimeter wave band," *Eng. Sci. Technol. Int. J.*, vol. 35, Nov. 2022, Art. no. 101129.

[38] L. Chen and X. Zhang, "Modification the surface quality and mechanical properties by laser polishing of Al/PLA part manufactured by fused deposition modeling," *Appl. Surf. Sci.*, vol. 492, pp. 765–775, Oct. 2019.

[39] R. Salazar, F. Pizarro, D. Vasquez, and E. Rajo-Iglesias, "Assessment of 3D-printed waveguides using conductive filaments and a chloroform-based smoothing process," *Additive Manuf.*, vol. 51, Mar. 2022, Art. no. 102593.

[40] K. Kowsari et al., "Photopolymer formulation to minimize feature size, surface roughness, and stair-stepping in digital light processing-based three-dimensional printing," *Additive Manuf.*, vol. 24, pp. 627–638, Dec. 2018.

[41] P. E. Degarmo, J. T. Black, and R. A. Kohser, *DeGarmo's Materials and Processes in Manufacturing*, 10th ed. Hoboken, NJ, USA: Wiley, 2007.

[42] K. Lomakin, G. Gold, and K. Helmreich, "Analytical waveguide model precisely predicting loss and delay including surface roughness," *IEEE Trans. Microw. Theory Techn.*, vol. 66, no. 6, pp. 2649–2662, Jun. 2018.

[43] D. M. Pozar, *Microwave Engineering*, 4th ed. Hoboken, NJ, USA: Wiley, 2012.

[44] G. Gold and K. Helmreich, "A physical surface roughness model and its applications," *IEEE Trans. Microw. Theory Techn.*, vol. 65, no. 10, pp. 3720–3732, Oct. 2017.

[45] V. Turgaliev et al., "Small-size low-loss bandpass filters on substrate-integrated waveguide capacitively loaded cavities embedded in low temperature co-fired ceramics," *J. Ceram. Sci. Technol.*, vol. 6, no. 4, pp. 305–314, 2015.

[46] M. Baranowski, L. Balewski, A. Lamecki, and M. Mrozowski, "Fast design optimization of waveguide filters applying shape deformation techniques," in *Proc. 24th Int. Microw. Radar Conf. (MIKON)*, Sep. 2022, pp. 1–4.

[47] (2023). *InventSim-Software for RF, Microwave Engineering and Computational Electromagnetics*. Accessed: Jul. 1, 2023. [Online]. Available: https://inventsim.com/

[48] M. Lumia et al., "Additive manufacturing of RF waveguide components," in *Recent Microwave Technologies*, A. Kishk and K. H. Yeap, Eds. Rijeka, Croatia: IntechOpen, 2022.

[49] *Renishaw AM 400 Additive Manufacturing System*. Accessed: Jul. 1, 2023. [Online]. Available: https://www.renishaw.com/

[50] *Renishaw RenAM 500 Series Stainless Steel 316L (1.4404) Material Data Sheet*. Accessed: Jul. 1, 2023. [Online]. Available: https://www.renishaw.com/en/material-and-safety-data-sheets-additive-manufacturing–17862

[51] (2023). *Keysight Vector Network Analyzer Uncertainty Calculator Software*. Accessed: Jul. 1, 2023. [Online]. Available: https://www.keysight.com/es/en/lib/software-detail/computer-software/downloadable-vector-network-analyzer-uncertainty-calculator-1000000418epsgsud.html

[52] B. Al-Juboori et al., "Lightweight and low-loss 3-D printed millimeter-wave bandpass filter based on gap-waveguide," *IEEE Access*, vol. 7, pp. 2624–2632, 2019.

[53] X. B. Shang et al., "W-band waveguide filters fabricated by laser micromachining and 3-D printing," *IEEE Trans. Microw. Theor. Tech.*, vol. 64, no. 8, pp. 2572–2580, Aug. 2016.

[54] P. A. Booth and E. V. Lluch, "Realising advanced waveguide bandpass filters using additive manufacturing," *IET Microw., Antennas Propag.*, vol. 11, no. 14, pp. 1943–1948, Nov. 2017.

[55] M. Salek et al., "W-band waveguide bandpass filters fabricated by micro laser sintering," *IEEE Trans. Circuits Syst. II, Exp. Briefs*, vol. 66, no. 1, pp. 61–65, Jan. 2019.

**Jakub Sorocki** (Senior Member, IEEE) received the M.Sc., Ph.D., and D.Sc. degrees in electrical engineering from the AGH University of Krakow, Krakow, Poland, in 2013, 2018, and 2023, respectively.

Since 2011, he has been with the Microwave Research Group, AGH University of Krakow. Since 2023, he has been an Associate Professor at the Institute of Electronics, AGH University of Krakow. His research interests are focused on the development of low-loss and high-performance microwave circuits in waveguide and strip transmission line technique for industrial applications taking advantage of additive and subtractive fabrication technologies.

**Ilona Piekarz** (Senior Member, IEEE) received the M.Sc., Ph.D., and D.Sc. degrees in electrical engineering from the AGH University of Krakow, Krakow, Poland, in 2013, 2018, and 2023, respectively.

Since 2011, she has been with the Microwave Research Group, AGH University of Krakow. Since 2023, she has been an Associate Professor at the Institute of Electronics, AGH University of Krakow. Her research interests are focused on the development of sensors and measurement systems in strip transmission line techniques for industrial and biomedical applications that take advantage of both subtractive and additive fabrication techniques.

**Michal Baranowski** (Graduate Student Member, IEEE) received the B.Sc. and M.Sc. degrees in electronic and telecommunication engineering from the Gdańsk University of Technology, Gdańsk, Poland, in 2020 and 2021, respectively, where he is currently pursuing the Ph.D. degree at the Doctoral School.

His research interests include computational electromagnetics, microwave filter design, and optimization techniques.

**Adam Lamecki** (Senior Member, IEEE) received the M.S.E.E. and Ph.D. degrees in microwave engineering from the Gdańsk University of Technology (GUT), Gdańsk, Poland, in 2002 and 2007, respectively.

In 2007, he is the Co-Founded EM Invent, Gdańsk, a Spin-Off Company, which develops an electromagnetic field simulator InventSim, where he was the Chief Technology Officer. Since 2019, he has been an Associate Professor with the Department of Microwave and Antenna Engineering, GUT. His research interests include filter design and optimization techniques, surrogate models and their application to the computer aided design of microwave devices, and computational electromagnetics.

**Alberto Cattenone**, photograph and biography not available at the time of publication.

**Stefania Marconi**, photograph and biography not available at the time of publication.

**Gianluca Alaimo**, photograph and biography not available at the time of publication.

**Nicolo Delmonte** (Member, IEEE) received the bachelor's degree in electronics and computer engineering and the master's degree in electronic engineering from the University of Pavia, Pavia, Italy, in February 2015 and in September 2017, respectively, and the Ph.D. degree from the Microwave Laboratory, in 2020.

His research interests include microwave components in substrate integrated waveguide (SIW) technology and RF circuit design.

**Lorenzo Silvestri** (Member, IEEE) received the M.Sc. degree in electronic engineering–telecommunication system curriculum and the Ph.D. degree in electronic, electrical and computer engineering from the University of Pavia, Pavia, Italy, in 2014 and 2019, respectively.

After the Ph.D., until September 2020, he held a post-doctoral position at the University of Pavia. He is currently a Researcher at the University of Pavia. His research interests include the design of reconfigurable substrate integrated waveguide (SIW) components.

Dr. Silvestri was a recipient of a One-Year Post-Graduate Scholarship at the University of Pavia, in 2014.

**Maurizio Bozzi** (Fellow, IEEE) received the Ph.D. degree in electronics and computer science from the University of Pavia, Pavia, Italy, in 2000.

He is currently a Full Professor of electromagnetic fields at the University of Pavia. His research interests include concern computational electromagnetics, substrate integrated waveguide technology, and the use of novel materials and fabrication technologies for microwave circuits.

Prof. Bozzi is the 2024 President of the IEEE Microwave Theory and Technology Society (MTT-S).